Advanced Fiber Materials (2024) 6:810–824
https://doi.org/10.1007/s42765-024-00380-1

RESEARCH ARTICLE

Efficient and Homogenous Precipitation of Sulfur Within a 3D Electrospun Heterocatalytic Rutile/Anatase TiO_{2-x} Framework in Lithium–Sulfur Batteries

Ping Feng[1] · Kang Dong[1] · Yaolin Xu[1] · Xia Zhang[1] · Haojun Jia[2] · Henrik Prell[3] · Michael Tovar[3] · Ingo Manke[1] · Fuyao Liu[4] · Hengxue Xiang[4] · Meifang Zhu[4] · Yan Lu[1,5,6]

Received: 10 October 2023 / Accepted: 16 January 2024 / Published online: 18 March 2024

Abstract

Lithium–sulfur (Li–S) batteries can potentially outperform state-of-the-art lithium-ion batteries, but their further development is hindered by challenges, such as poor electrical conductivity of sulfur and lithium sulfide, shuttle phenomena of lithium polysulfides, and uneven distribution of solid reaction products. Herein, free-standing carbon nanofibers embedded with oxygen-deficient titanium dioxide nanoparticles (TiO_{2-x}/CNFs) has been fabricated by a facile electrospinning method, which can support active electrode materials without the need for conductive carbon and binders. By carefully controlling the calcination temperature, a mixed phase of rutile and anatase was achieved in the TiO_{2-x} nanoparticles. The hybridization of anatase/rutile TiO_{2-x} and the oxygen vacancy in TiO_{2-x} play a crucial role in enhancing the conversion kinetics of lithium polysulfides (LiPSs), mitigating the shuttle effect of LiPSs, and enhancing the overall efficiency of the Li–S battery system. Additionally, the free-standing TiO_{2-x}/CNFs facilitate uniform deposition of reaction products during cycling, as confirmed by synchrotron X-ray imaging. As a result of these advantageous features, the TiO_{2-x}/CNFs-based cathode demonstrates an initial specific discharge capacity of 787.4 mAh g^{-1} at 0.5 C in the Li–S coin cells, and a final specific discharge capacity of 584.0 mAh g^{-1} after 300 cycles. Furthermore, soft-packaged Li–S pouch cells were constructed using the TiO_{2-x}/CNFs-based cathode, exhibiting excellent mechanical properties at different bending states. This study presents an innovative approach to developing free-standing sulfur host materials that are well suited for flexible Li–S batteries as well as for various other energy applications.

Keywords Li–S batteries · TiO_{2-x} · Electrospinning · Heterocatalyst · X-ray tomography

✉ Hengxue Xiang
hengxuexiang@dhu.edu.cn

✉ Yan Lu
yan.lu@helmholtz-berlin.de

[1] Institute of Electrochemical Energy Storage, Helmholtz-Zentrum Berlin für Materialien und Energie, 14109 Berlin, Germany

[2] Department of Chemistry, Massachusetts Institute of Technology, Cambridge, MA 02139, USA

[3] Department Structure and Dynamics of Energy Materials, Helmholtz-Zentrum Berlin für Materialien und Energie GmbH, 14109 Berlin, Germany

[4] State Key Laboratory for Modification of Chemical Fibers and Polymer Materials, College of Materials Science and Engineering, Donghua University, Shanghai 201620, People's Republic of China

[5] Institute for Technical and Environmental Chemistry, Friedrich-Schiller-Universität Jena, 07743 Jena, Germany

[6] Helmholtz Institute for Polymers in Energy Applications Jena (HIPOLE Jena), 07743 Jena, Germany

Introduction

Since their commercialization in the 1990s, lithium-ion batteries (LIBs) have dominated the worldwide battery market in the portable electronics sector, and recently become the indispensable and crucial systems for electric vehicles (EV) [1–3]. However, current LIBs have gradually reached its theoretical capacity limit and cannot meet the ever-increasing demand for new applications such as consumer electronics [4–6]. As an alternative, lithium–sulfur (Li–S) batteries have gradually come into the limelight as advanced energy storage systems since their discovery in 1960s, due to their ultrahigh theoretical energy density (up to 2600 Wh kg^{-1}) and low cost [7–11].

However, several significant challenges hinder the commercialization of Li–S batteries. First, the poor electrical conductivity of sulfur (*ca.* 5×10^{-30} S cm^{-1} at room temperature) and its lithiation product (Li_2S) leads to sluggish kinetics and low utilization of active materials [12–16]. Second, a series of soluble lithium polysulfides (LiPSs, i.e., Li_2S_x, $4 \leq \times \leq 8$) intermediates generated during charging and discharging processes could bring about the crossover of LiPSs, i.e., "shuttle" phenomenon, leading to severe capacity fading and low Coulombic efficiency [17–21]. Finally, the dissolution of intermediate LiPSs induces the inhomogeneous redistribution of solid products at the active surfaces, causing the aggregation of solid sulfur species, the passivation of the electrode/electrolyte interface, and large overpotential during the solid–liquid–solid conversion [22–25].

A series of solid–liquid–solid conversions, corresponding to the (re)formation of sulfur–LiPSs–Li_2S, are involved in the redox reaction of sulfur in Li–S batteries. Therefore, the interfaces in the sulfur cathode composite, where the (re)deposition occurs, play an important role in regulating the morphology of the (re)deposited sulfur. Using 3D nonwoven carbon (NWC), Zielke et al. showed that dissolved sulfur during the first discharge could propagate within the 3D carbon matrix with cycling via back diffusion [26]. The inhomogeneous deposition and redistribution of sulfur during cycling could be attributed to the poor affinity of the non-polar carbon for LiPSs. Similarly, an increase in the volume fraction of sulfur toward the current collector was observed during cycling in Ketjen Black@Sulfur composite electrodes due to the higher electrical conductivity of the current collector [27]. The inhomogeneous deposition of sulfur results in sulfur aggregates forming at limited nucleation sites, leading to a low sulfur utilization ratio. Therefore, regulating the precipitation of sulfur on different reactive interfaces would be critical to homogenize the (re) deposition of sulfur and improve the cycling stability of Li–S batteries.

To address the above-mentioned issues and improve the electrochemical performance of Li–S batteries, many strategies have been proposed, such as building a conductive framework to confine sulfur [28–31], functionalizing separators [32], or adding interlayers [33]. Among these, the strategy of utilizing carbon-based electrodes as host materials for sulfur is widely used, but fails to effectively confine sulfur during long-term operation due to the insufficient physical and chemical adsorption between polar LiPSs and non-polar carbon. To address this issue, coating the carbon matrices with polar materials, such as titanium dioxide (TiO_2), is proposed [34–37], which can strongly anchor and efficiently constrain LiPSs and therefore reduces the dissolution of LiPSs and improves the cycling performance [38]. TiO_2 is one representative transition metal oxide, which is stable, abundant, ecofriendly, and safe. Many studies indicate that the electrochemical performance of lithium–sulfur batteries can be greatly improved with TiO_2 as sulfur immobilizers, due to the strong adsorption of sulfur by Ti–O bond [39, 40]. However, pristine TiO_2, as a semiconductor, has limited electrical conductivity and exhibits poor rate performance and cycling stability [41].

Creating cation vacancies is a powerful way to improve electrochemical performance via lowering diffusion energy barriers, providing extra intercalation sites, and enhancing electrode kinetics [42]. However, cation vacancies are rarely studied in the research field due to their difficult characterization and the limited availability of suitable host materials with such defects [40]. Recently, oxygen-deficient TiO_2 has gained attention, because oxygen vacancies can not only act as shallow donors, narrowing the band gap (Eg), raising the density of states below the Fermi level, and facilitating charge transfer in TiO_2 lattice, but also enhance the affinity of TiO_2 toward LiPSs and simultaneously catalyze their redox conversion by propelling the electron/Li^+ transport on the vacancy-enriched surface [43]. For instance, Liang et al. designed hydrogen-reduced TiO_2 as a sulfur host and achieved long cycle life and high capacity compared to that of pristine TiO_2 due to the significantly improved electrical conductivity of oxygen-deficient TiO_2 [44]. Later on, oxygen-deficient anatase TiO_2 nanosheets, synthesized by partially reducing TiO_2 nanosheets in the $NaBH_4$ solution, were reported by Wu and co-workers [45]. The oxygen vacancies not only promote electronic transfer but also act as more effective polysulfide reservoirs to reduce the dissolution of LiPSs [46]. As a result, Li–S coin cells based on oxygen-deficient anatase TiO_2 nanosheets maintained a high initial specific discharge capacity of 1277.1 mAh g^{-1} at 0.1 C, and a stable Coulombic efficiency of approximately 99.2% after the first five cycles. However, these electrodes are based on TiO_2 particles in the powder form, which requires the addition of conductive agents, binders, and current collectors during the electrode

fabrication process, leading to complexities in achieving optimal electrode performance and stability. Moreover, the development of self-supporting electrodes to increase energy density and enable flexible battery applications remains a great challenge.

Herein, we successfully synthesized oxygen-deficient titanium dioxide nanoparticles embedded in free-standing carbon nanofibers (TiO_{2-x}/CNFs) through electrospinning followed by calcination in an Ar/H_2 atmosphere. By controlling the calcination temperature, a hybrid anatase/rutile phase of TiO_2 was obtained, which exhibits superior polysulfide adsorbability and catalytic effects in Li–S batteries. The presence of oxygen vacancies in TiO_{2-x}/CNFs, created by hydrogen reduction significantly improves the electrical conductivity of TiO_2 nanoparticles in the TiO_{2-x}/CNFs. This, in turn, fastens electron transfer from the catalytic center to the conductive carbon matrix and enhances the adsorption ability of polysulfides in Li–S batteries. Meanwhile, the electrospun CNFs establish an electrically conductive framework, ensuring efficient electron transport within the electrode. Furthermore, the free-standing nature of the TiO_{2-x}/CNFs-based electrodes allows them to support active electrode materials without the need for conductive carbon and binders. The soft-packaged Li–S pouch cell was constructed on the TiO_{2-x}/CNFs-based cathode, demonstrating excellent mechanical properties even under different bending states. This characteristic is advantageous for scaling production, reducing costs, and constructing flexible batteries suitable for emerging wearable electronics and flexible displays.

Results and Discussion

The free-standing TiO_{2-x}/CNFs are prepared by a facile two-step strategy, as shown in Fig. 1a. First, a certain amount of tetrabutyl titanate (TBT), polyvinyl pyrrolidone (PVP), and acetic acid is dissolved in ethanol and stirred for 5 h to get a yellow solution, and this solution is electrospun to a white membrane (Fig. S1). Second, after stabilization at 60 °C overnight, the white membrane is calcined at 600 °C for 2 h under Ar/H_2 (5%) atmosphere to get the black TiO_{2-x}/CNFs. The TiO_{2-x}/CNFs membrane shows excellent flexibility after calcination and can be cut into self-supporting electrodes and used directly as host materials for Li–S batteries (Fig. 1b). The free-standing nature of the TiO_{2-x}/CNFs-based electrodes allows them to support active electrode materials without the need for conductive carbon and binders. Such a self-supporting structure not only enhances the efficiency of electrode production but also contributes to cost reduction [47, 48].

Detailed morphological observations of the as-obtained TiO_{2-x}/CNFs have been conducted by applying Scanning Electron Microscope (SEM) and Transmission Electron Microscope (TEM) measurements at different magnifications. SEM and TEM images shown in Fig. 1c–e reveal that the TiO_{2-x}/CNFs maintain a continuous one-dimensional fibrous geometry after calcination. The diameter distribution (Fig. S2) measured from the SEM images shows that the diameter of most nanofibers is in the range of 300–600 nm. With the aid of high-resolution TEM, ultrasmall TiO_{2-x} nanoparticles with size of 5–10 nm can be clearly seen, which are homogenously embedded into the CNFs, as shown in Fig. 1f. The high-resolution TEM image of the TiO_{2-x}/CNFs in Fig. 2g shows the adjacent lattice of 0.357 nm (orange area), 0.324 nm (black area), and 0.246 nm (black area), corresponding to the (101) planes of anatase TiO_2, and (110) and (101) planes of rutile TiO_2, respectively [49]. Figure 2g1, g2 shows the corresponding fast Fourier-transform pattern of the anatase and rutile TiO_2, respectively, confirming the well-crystallized structure. Elemental mapping images by energy-dispersive X-ray spectrometry (EDS) show that Ti elements are located within the CNFs (Fig. 1h). Note that a carbon tape was used to fix TiO_{2-x}/CNFs on the sample holder for SEM measurement, which gives a strong carbon signal in the C mapping image in Fig. 1h. From the TEM and EDS mapping results, we can conclude that TiO_{2-x} nanoparticles with size of 5–10 nm are homogenously embedded into the CNFs without aggregation, which can not only improve the electrical conductivity, thus improving the kinetic behaviors of soluble LiPSs, but also afford strong interaction with LiPSs due to abundant exposed active sites [44]. Figure S3 shows the SEM and TEM images of the pure TiO_2 nanofibers prepared by calcination of TBT/PVP nanofibers at 600 °C for 2 h under Air. The surface of the TiO_2 nanofiber without carbon becomes rough and the cross-section of the nanofibers shows a lot of TiO_2 nanoparticles. It is worth noting that the TiO_{2-x}/CNFs maintain the free-standing property, while the pure TiO_2 nanofibers cannot be free-standing (Fig. S4), indicating the vital role of the carbon phase in maintaining the structural stability. In addition, two control samples were prepared as reference. First of all, free-standing CNFs embedded with titanium dioxide nanoparticles (TiO_2/CNFs) were prepared as a control sample by calcination of TBT/PVP nanofibers at 600 °C for 2 h under Ar. The second control sample is CNFs, which were prepared with the same condition of TiO_{2-x}/CNFs without the addition of tetrabutyl titanate. The digital images and SEM images of TiO_2/CNFs and CNFs are shown in Fig. S5a–d, respectively. The XRD pattern of the TiO_2/CNFs (Fig. S6) shows the mixed phase of anatase and rutile, which is similar with that of TiO_{2-x}/CNFs.

X-ray diffraction (XRD) was conducted to study the phase transformation of the TiO_2 nanoparticles during calcination of TBT/PVP nanofibers at various temperatures under Ar/H_2 (5.0%) atmosphere. In the XRD pattern (Fig.

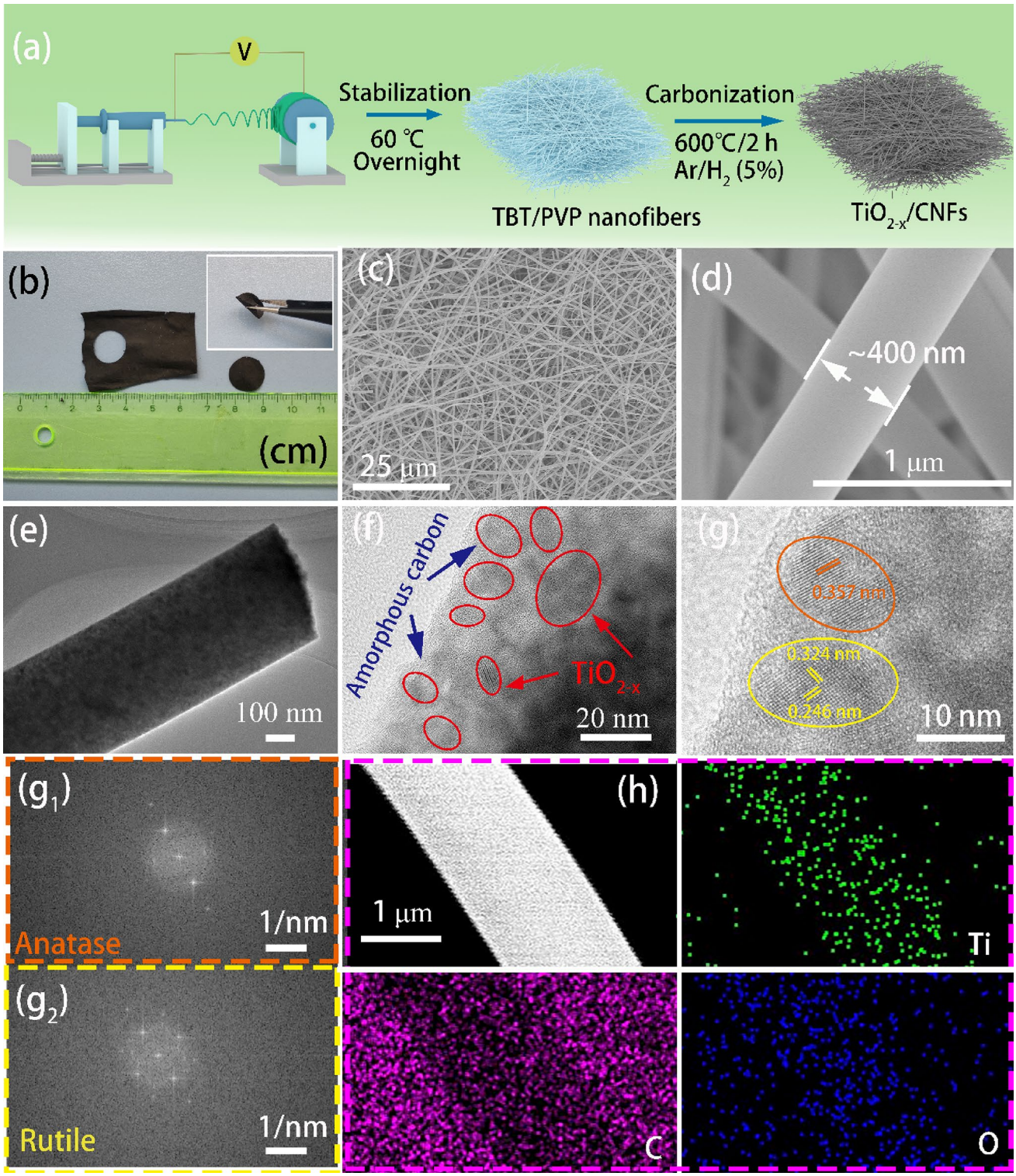

Fig.1 **a** Schematic illustration of the synthesis process of the TiO_{2-x}/CNFs. **b** Digital image of the as-prepared TiO_{2-x}/CNFs. **c**, **d** SEM images of the TiO_{2-x}/CNFs. **e**–**g** TEM and HRTEM images of the TiO_{2-x}/CNFs. **h** SEM image and the corresponding Ti, O, and C elemental mapping images of the TiO_{2-x}/CNFs

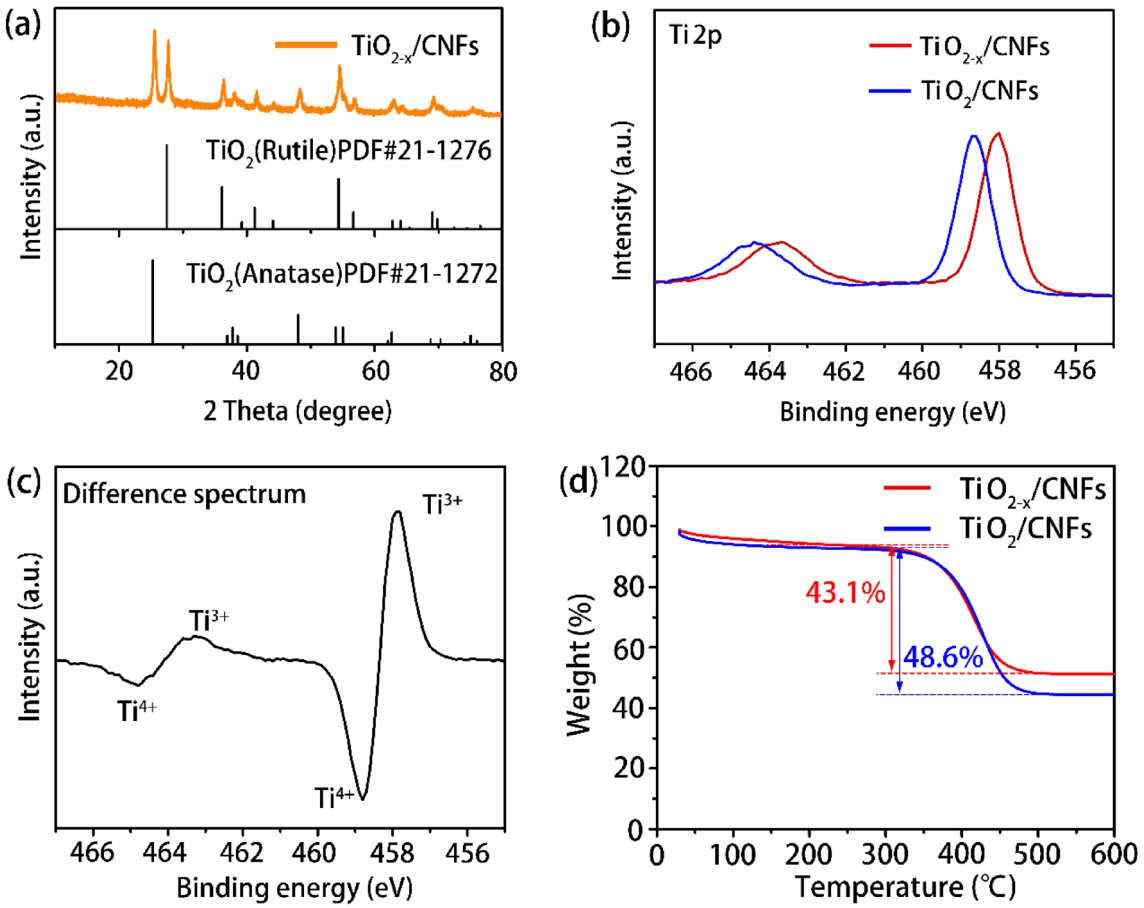

Fig. 2 **a** XRD pattern of the TiO_{2-x}/CNFs. **b** Ti 2p XPS spectra of the TiO_{2-x}/CNFs and TiO_2/CNFs and **c** the corresponding Ti 2p difference spectrum. **d** TGA spectra of the TiO_{2-x}/CNFs and TiO_2/CNFs under air from room temperature to 600 °C at a ramping rate of 10.0 °C min^{-1}

S7), a pure anatase phase of TiO_2 was obtained for the sample calcined at 500 °C (denoted at TiO_{2-x}/C 500). As the calcination temperature increased to 550 °C, the anatase remained as the main phase. In addition, a small new peak appeared at 2θ of 27.8°, indicating the emergence of the rutile phase of TiO_2. The XRD pattern of the sample calcined at 600 °C clearly showed new peaks at 2θ of 27.8°, 36.4°, and 54.8°, belonging to the (110), (101), and (211) of the rutile phase, respectively, confirming the coexistence of anatase and rutile phases in the TiO_{2-x}/CNFs. Further increasing the calcination temperature to 650 °C and 700 °C, the peaks corresponding to the rutile phase (at 2θ of 27.8°, 36.4°, 54.8°) became predominant, while the peaks from the anatase phase (at 2θ of 25.6°, 38.2°, 48.4°) gradually disappeared. At 800 °C, all peaks associated with the anatase phase vanished, and pure rutile phase of TiO_2 was obtained (denoted as TiO_{2-x}/C 800). It is worth noting that the calcination temperature also influences the free-standing property of the TiO_{2-x}/CNFs. TiO_{2-x}/C 800 was not free-standing (Fig. S8a), unlike TiO_{2-x}/C 500 and TiO_{2-x}/CNFs. SEM and TEM images of the TiO_{2-x}/C 800, as shown in Fig. S8b–d, revealed a porous structure of the nanofiber resulting from the phase transformation from anatase to rutile. These results demonstrate that the phase of TiO_2 nanoparticles and the free-standing property of TiO_{2-x}/CNFs can be effectively controlled by calcination temperature.

Figure 2a displays the XRD pattern of the TiO_{2-x}/CNFs calcined at 600 °C for 2 h, revealing a hybrid anatase/rutile phase. Quantitative phase analysis using the TOPAS software package (Bruker, Version 7) of this pattern indicated an anatase and rutile content of around 47 and 53%, respectively, in the TiO_{2-x} nanoparticles. X-ray photoelectron spectroscopy (XPS) is used to study the valence states of the TiO_{2-x}/CNFs. The deconvoluted Ti 2p XPS spectrum of the TiO_{2-x}/CNFs (Fig. 2b) exhibits two main peaks located at 464.2 and 458.5 eV, corresponding to the 2p1/2 and 2p3/2 components of Ti^{4+} in the TiO_{2-x}/CNFs lattice, respectively [50]. However, compared with the Ti 2p XPS spectrum of the TiO_2/CNFs, the Ti^{4+} peak of the TiO_{2-x}/CNFs shifts to the lower binding energy, and the difference spectrum of the Ti 2p XPS spectrum (Fig. 2c) clearly indicates that part of the Ti^{4+} in the TiO_{2-x}/CNFs is reduced to Ti^{3+} due to

hydrogen reduction [44]. Electron paramagnetic resonance (EPR) spectroscopy is used to investigate the coordination of oxygen atoms. As shown in Fig. S9, the peak intensity at $g = 2.0$ of the TiO_{2-x}/CNFs sample is much higher than that of TiO_2/CNFs. The result manifests the increase in the number of unpaired electrons, which is related to the presence of Ti^{3+} and oxygen vacancy in TiO_2. The oxygen vacancies are likely to be more abundant in the rutile phase than in the anatase phase. Previous research employing first-principles calculations [51] reported that surface oxygen vacancies are more likely to occur on the rutile TiO_2 (110) surface due to the larger formation energy for surface oxygen vacancies on the anatase TiO_2 (101) surfaces. It is well known that hydrogen atmosphere can induce surface oxygen vacancies, which not only improve electrical conductivity but also accelerate polysulfide conversion reaction [41, 45, 46]. Thermogravimetry analysis (TGA) was conducted in air from room temperature to 600 °C at a ramping rate of 10.0 °C min^{-1} to measure the carbon content inside the nanofibers. TGA spectra of the TiO_{2-x}/CNFs and TiO_2/CNFs (Fig. 2d) exhibit slight weight loss below 300 °C due to the gradual evaporation of the adsorbed water. Subsequently, significant weight loss occurs after 300 °C, primarily originating from the carbon oxidation. Above 500 °C, both samples show no weight change, indicating complete oxidation of the carbon in the nanofibers to carbon dioxide [52]. The calculated carbon content is approximately ~ 43.1 wt% for TiO_{2-x}/CNFs and ~ 48.6 wt% for TiO_2/CNFs. The N_2 adsorption/desorption isotherm profile and corresponding pore size distribution plot (Fig. S10) demonstrate the porous nature of the as-prepared TiO_{2-x}/CNFs. The Brunauer–Emmett–Teller (BET)-specific surface area of the TiO_{2-x}/CNFs is 9.97 m^2 g^{-1}, with most pores distributed around 3.0 nm. This porous structure mainly arises from the decomposition of PVP during the calcination process [53, 54].

It has been reported that the mixed phase of anatase and rutile TiO_2 exhibits a synergistic adsorption effect, effectively suppressing the shuttle effect of LiPSs [43]. To investigate the adsorbability of polysulfides and the catalytic effect of the anatase TiO_2 (TiO_{2-x}/C 500), rutile TiO_2 (TiO_{2-x}/C 800), and hybrid rutile/anatase (TiO_{2-x}/CNFs), a series of comparisons were conducted (Fig. 3). The visual discrimination of LiPSs onto TiO_{2-x}/CNFs, TiO_{2-x}/C 800, and TiO_{2-x}/C 500 (Fig. 3a) was carried out by adding 20 mg

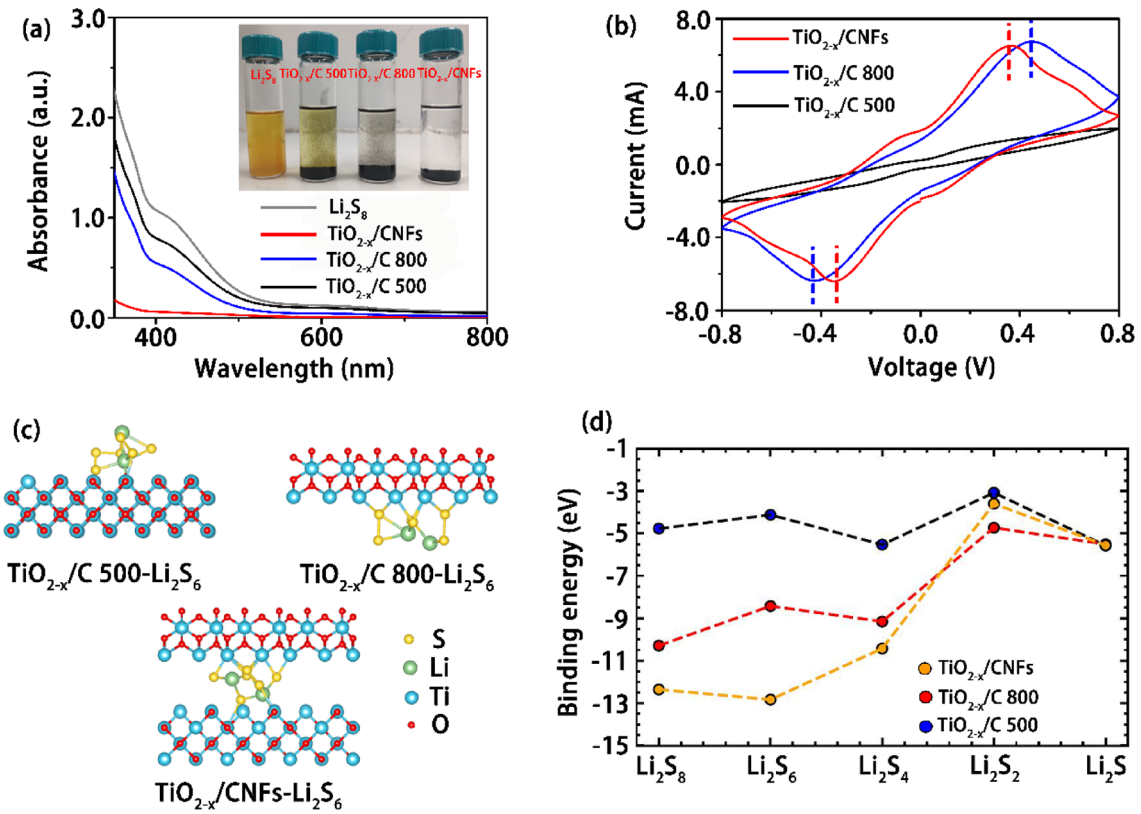

Fig. 3 **a** UV–Vis absorption spectra of the Li_2S_8 electrolyte after mixing with TiO_{2-x}/CNFs, TiO_{2-x}/C 800, and TiO_{2-x}/C 500 for 1 h. Inset: photographs of the Li_2S_8 solutions (4 mL, 2 mM, dissolved in DME/DOL) after mixing with 20 mg of different adsorbers for 1 h. **b** Li_2S_8 symmetric cells with TiO_{2-x}/CNFs, TiO_{2-x}/C 800, and TiO_{2-x}/C 500 as electrodes with a scan rate of 10 mV s^{-1} in a voltage range of − 0.8 to 0.8 V. **c** Optimized configurations for the binding of Li_2S_6 to TiO_{2-x}/CNFs, TiO_{2-x}/C 800, and TiO_{2-x}/C 500. **d** Binding energy (in eV) of the Li_2S_x cluster adsorption on TiO_{2-x}/CNFs, TiO_{2-x}/C 800, and TiO_{2-x}/C 500

of each host material to a Li_2S_8 solution (4 mL, 2 mM, dissolved in DOL/DME). After aging for 1 h, the color of the supernatant liquid containing TiO_{2-x}/CNFs, TiO_{2-x}/C 800, and TiO_{2-x}/C 500 faded compared to the original solution, indicating their ability to adsorb LiPSs. Ultraviolet–visible (UV–Vis) measurement of the Li_2S_8 solution after the polysulfides adsorption test confirmed that the supernatant solution treated with TiO_{2-x}/CNFs showed the lowest absorption in the wavelength range of 350–500 nm, indicating the highest polysulfide adsorbability of the hybrid rutile/anatase TiO_{2-x}. The catalytic effect of the TiO_{2-x}/CNFs, TiO_{2-x}/C 800, and TiO_{2-x}/C 500 on polysulfide redox reaction was investigated using cyclic voltammetry (CV) of Li_2S_8 symmetrical cells. The CV was performed at a scan rate of 10 mV s^{-1} in a voltage range from − 0.8 to 0.8 V [55, 56]. Figure 3b shows the current response of the Li_2S_8 symmetrical cells using different electrodes. The area under the CV plots is directly proportional to the total charge passed during the cyclic scan, which corresponds to the charge and discharge capacity of the Li_2S_8 symmetrical cells. The larger area of the CV plots in the TiO_{2-x}/C 800 and TiO_{2-x}/CNFs electrodes compared to the TiO_{2-x}/C 500 electrode indicates their faster redox kinetics of LiPSs conversion reactions. This enhanced redox kinetics is likely attributed to both the improved electrical conductivity of carbon and the increased presence of oxygen vacancies resulting from their higher calcination temperatures. The polarization of the CV plots in the Li_2S_8 symmetrical cells reflects the overpotential during the redox reactions of LiPSs. It is measured as the difference between the oxidation and reduction peaks in the CV plot. The TiO_{2-x}/CNFs electrode exhibited smaller polarization compared to that of the TiO_{2-x}/C 800 electrodes, indicating that the hybrid anatase/rutile TiO_{2-x} enhances the LiPSs redox kinetics [57]. These findings suggest that the hybrid rutile/anatase TiO_{2-x} nanoparticles in TiO_{2-x}/CNFs offer superior polysulfide adsorbability and catalytic effects, making them a promising candidate as the sulfur host in lithium–sulfur batteries.

To understand the mutual influence of anatase (TiO_{2-x}/C 500) and rutile (TiO_{2-x}/C 800) on LiPSs species, the rutile/anatase heterojunction structure (TiO_{2-x}/CNFs) was constructed using the (110) slab of rutile and the (101) slab of anatase, with adjustments made to minimize lattice mismatch. Density functional theory (DFT) calculations were carried out to determine the relative energies on a series of representative LiPSs species (Li_2S, Li_2S_2, Li_2S_4, Li_2S_6, and Li_2S_8) binding on TiO_{2-x}/CNFs, TiO_{2-x}/C 800, and TiO_{2-x}/C 500, respectively. To quantitatively determine the interaction between the surface and adsorbers, we computed the binding energies of flakes. E(total) is the total energy of surfaces with corresponding adsorbers, E(sur) is the energy of surface (TiO_{2-x}/CNFs, TiO_{2-x}/C 800, and TiO_{2-x}/C 500), and E(ads) is the energy of Li_2S_x ($x = 1$, 2, 4, 6, and 8) cluster in gas phase. The binding energy is evaluated by Eq. (1)

$$E(\text{binding}) = E(\text{total}) - E(\text{sur}) - E(\text{ads}). \quad (1)$$

The simulation results are shown in Fig. 3c, d and Table 1, indicating that the TiO_{2-x}/CNFs is energetically more favorable (with lower binding energy) with LiPSs species comparing with LiPSs species adsorption on the surface of TiO_{2-x}/C 500 and TiO_{2-x}/C 800, respectively. The binding energy of TiO_{2-x}/CNFs with LiPSs species is generally lower than that of TiO_{2-x}/C 500 and TiO_{2-x}/C 800 during the discharge process. The binding energy of TiO_{2-x}/CNFs is significantly lower than that of TiO_{2-x}/C 500 and TiO_{2-x}/C 800 for long-chain LiPSs species (Li_2S_4, Li_2S_6, and Li_2S_8). However, the adsorption energy of TiO_{2-x}/CNFs, TiO_{2-x}/C 800, and TiO_{2-x}/C 500 is similar for short-chain LiPSs species (Li_2S and Li_2S_2), consistent with the previous reports [49]. The binding energies in this work are relatively larger than previous reports due to the size effect [58] caused by the supercell of TiO_{2-x}/CNFs, TiO_{2-x}/C 500, and TiO_{2-x}/C 800. The final product Li_2S shows almost the same binding energy with the TiO_{2-x}/C 500 surface (− 5.566 eV), TiO_{2-x}/C 800 surface (− 5.502 eV), and TiO_{2-x}/CNFs surface (− 5.549 eV). The results above indicate that, in comparison with TiO_{2-x}/C 500 and TiO_{2-x}/C 800, TiO_{2-x}/CNFs are more energetically favorable for the adsorption of long-chain LiPSs species (Li_2S_4, Li_2S_6, and Li_2S_8), while exhibiting similar performance for the short-chain LiPSs species (Li_2S and Li_2S_2). Therefore, the sample calcined at 600 °C containing mixed rutile and anatase phase with a ratio of roughly 1:1, which is expected to exhibit maximized synergistic effect of the hybrid phase, has been chosen as the host materials for further electrochemical studies in this work.

To investigate the function of oxygen vacancy in TiO_2 nanoparticles and CNFs in TiO_{2-x}/CNFs regarding LiPSs adsorption ability and catalytic effects for the conversion reaction of LiPSs, a series of experiments were carried out. The adsorption ability of LiPSs on TiO_{2-x}/CNFs, TiO_2/CNFs, and CNFs was compared by adding 20 mg of each host material to a Li_2S_8 solution (4 mL, 2 mM, dissolved in DME/DOL). The digital image in Fig. 4a shows the appearance of all samples after aging for 4 h. The color of the

Table 1 Binding energy (in eV) of the Li_2S_x cluster adsorption on TiO_{2-x}/CNFs, TiO_{2-x}/C 800, and TiO_{2-x}/C 500

	Li_2S_8	Li_2S_6	Li_2S_4	Li_2S_2	Li_2S
TiO_{2-x}/CNFs	− 12.356	− 12.833	− 10.419	− 3.588	− 5.549
TiO_{2-x}/C 800	− 10.286	− 8.419	− 9.151	− 4.722	− 5.502
TiO_{2-x}/C 500	− 4.765	− 4.115	− 5.520	− 3.071	− 5.566

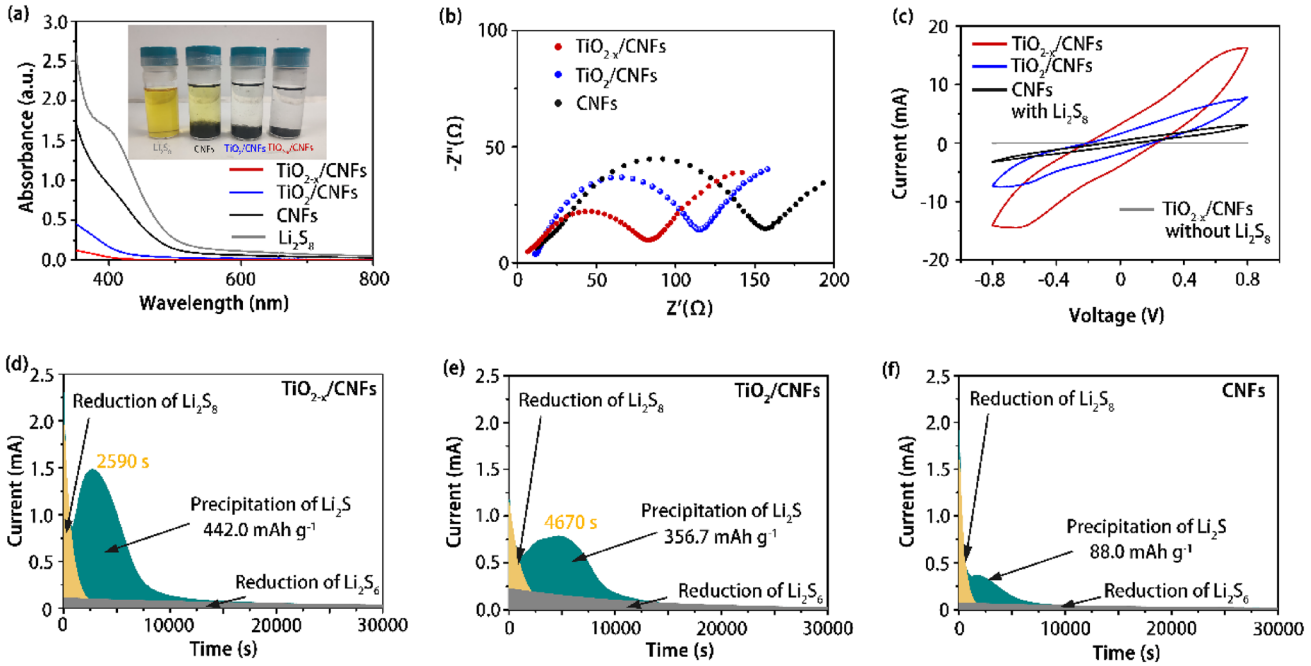

Fig. 4 **a** UV–Vis absorption spectra of the Li_2S_8 electrolyte after mixing with TiO_{2-x}/CNFs, TiO_2/CNFs, and CNFs. Inset: graphs of the Li_2S_8 solutions (4 mL, 2 mM, dissolved in DME/DOL) after mixing with 20 mg of different adsorbers. **b** Nyquist plots of the TiO_{2-x}/CNFs, TiO_2/CNFs, and CNFs-based cathode before cycling. **c** Li_2S_8 symmetric cells with TiO_{2-x}/CNFs, TiO_2/CNFs, and CNFs as electrodes at a scan rate of 10 mV s^{-1}. Fitting of the current–time behavior for constant potentiostat discharge at 2.05 V on TiO_{2-x}/CNFs (**d**), TiO_2/CNFs (**e**), and CNFs (**f**)-based electrode

supernatant liquid after mixing with the TiO_{2-x}/CNFs, TiO_2/CNFs, and CNFs has faded compared to the original Li_2S_8 solution, indicating that all three can adsorb polysulfides. Notably, the color of the supernatant after mixing with the TiO_{2-x}/CNFs turns from yellow to colorless, indicating its strong adsorption capability compared to the TiO_2/CNFs and CNFs. The UV–Vis spectra of the supernatant solutions after mixing with different sample (Fig. 4a) confirm that the LiPSs concentration in the TiO_{2-x}/CNFs sample is notably reduced compared to the TiO_2/CNFs and CNFs. This demonstrates that the presence of oxygen vacancies could enhance the LiPSs adsorption ability. Figure 4b illustrates the Nyquist plots of the coin cells containing TiO_{2-x}/CNFs, TiO_2/CNFs, and CNFs-based cathodes before cycling. These plots show a compressed semicircle in the high-frequency region, representing the charge-transfer reaction process at the electrode/electrolyte interface, and a linear part in the low-frequency region, representing lithium diffusion in the bulk of the electrode. The smallest charge-transfer resistance of the TiO_{2-x}/CNFs-based cathode indicates the improved electrochemical performance in the TiO_{2-x}/CNFs electrode, which is caused by the improved electrical conductivity of TiO_{2-x}/CNFs caused by the oxygen vacancy in the TiO_{2-x} nanoparticles [59].

The catalytic effects of different host materials toward lithium polysulfides conversion were further studied using Li_2S_8 symmetric cells. Figure 4c shows the CV graph of different host materials with the Li_2S_8 solution and TiO_{2-x}/CNFs without the Li_2S_8 solution at a scan rate of 10 mV s^{-1} in a voltage range from − 0.8 to 0.8 V. The TiO_{2-x}/CNFs electrode, when not in contact with the Li_2S_8 solution, shows minimal current response, indicating that the double-layer capacitance has a negligible contribution to the overall current. However, when in contact with the Li_2S_8 solution, the TiO_{2-x}/CNFs electrode exhibits the most substantial current response among TiO_2/CNFs and CNFs. The significant increase in current is primarily attributed to the high electrical conductivity and catalytic effect of the TiO_{2-x} nanoparticles. To further investigate the catalytic effects of different host materials on Li_2S precipitation, we conducted a study on the nucleation and growth of solid Li_2S on different host materials using a potentiostatic technique (see Experimental section), as reported previously [55, 56]. Figure 4d–f display the discharge profile of TiO_{2-x}/CNFs, TiO_2/CNFs, and CNFs at a constant voltage of 2.05 V for 30,000 s, respectively. The area under the current graphs was analyzed using two exponential functions, corresponding to the reduction of Li_2S_8 and Li_2S_6, respectively, and a remaining peak corresponding to the precipitation of Li_2S. Notably, TiO_{2-x}/CNFs exhibited the highest Li_2S precipitation capacity (442.0 mAh g^{-1}), indicating its superior catalytic effect compared to that of TiO_2/CNFs (237.0 mAh g^{-1}) and

CNFs (88.0 mAh g^{-1}). Moreover, the current peak of TiO_{2-x}/CNFs occurred at around 2590 s, which is much earlier than the peak observed for TiO_2/CNFs located at approximately 4670 s. In contrast, CNFs showed no significant peak and exhibited a weak current response. The combination of the highest Li_2S precipitation capacity and the early occurrence time of the current peak for TiO_{2-x}/CNFs indicates that TiO_{2-x}/CNFs can effectively accelerate the conversion from Li_2S_4 to Li_2S [60]. This effect is attributed to the higher electrical conductivity and catalytic properties of the TiO_{2-x} nanoparticles present in the TiO_{2-x}/CNFs structure.

The electrochemical performances of the TiO_{2-x}/CNFs, TiO_2/CNFs, and CNFs-based cathodes were examined in Li–S coin cells with a sulfur loading of 2 mg cm^{-2} (10.0 µL 1 M Li_2S_8 catholyte). It is noted that the mass density of TiO_{2-x}/CNFs is 1 mg cm^{-2}, which was determined by dividing the mass of TiO_{2-x}/CNFs by the corresponding area, as shown in Fig. S11. Such low density of TiO_{2-x}/CNFs is corresponding to a high porosity for accommodating sulfur active material. This is advantageous over the reported carbon cloth-based sulfur electrodes, because the mass density of pristine carbon cloth stands at 13 mg cm^{-2}. Typically, carbon cloth requires post-treatment to introduce catalysts, enhancing polysulfide adsorption capability and catalytic effects, subsequently increasing the density of the carbon cloth. Therefore, TiO_{2-x}/CNFs, produced via electrospinning, are lightweight and contribute to reducing the inactive mass. Figure 5a illustrates the CV behavior of the TiO_{2-x}/CNFs-based cathode during the initial three cycles in the voltage window of 1.7 to 2.8 V vs. Li/Li^+. In each anodic scan, two characteristic peaks are observed at ~ 2.3 V and ~ 2.0 V, which can be attributed to the reduction of sulfur into soluble polysulfides (Li_2S_x, $4 \leq \times \leq 8$) and subsequently reduced to insoluble Li_2S_2 and Li_2S, respectively. During the cathodic scan, two prominent peaks are observed at ~ 2.3 V and ~ 2.4 V. The first peak corresponds to the oxidation of insoluble Li_2S to soluble polysulfides (Li_2S_x, $4 \leq \times \leq 8$), and the other peak is associated with the final oxidation of soluble polysulfides into elemental sulfur [61–64]. These peak shapes and locations remain unchanged during the rest of the cycles, indicating the excellent cycling stability of Li–S coin cells with the TiO_{2-x}/CNFs-based cathode. The galvanostatic charge–discharge (GCD) graphs of the Li–S coin cells based on TiO_{2-x}/CNFs at different current rates are presented in Fig. 5b. At various current rates, one typical charge plateau and two discharge plateaus can be observed, which are in good agreement with the CV results.

The cycling performance of the TiO_{2-x}/CNFs, TiO_2/CNFs, and CNFs-based cathodes at a current density of 0.1 C (1 C = 1675 mA g^{-1}) for 100 cycles is presented in Fig. 5c. The TiO_{2-x}/CNFs-based cathode demonstrates a specific discharge capacity of 1026.4 mAh g^{-1} during the first discharge process, and this capacity remains stable at 748.0 mAh g^{-1} after 100 cycles with high Coulombic efficiency (nearly 100%). In contrast, the TiO_2/CNFs and CNFs-based cathodes exhibit rapid capacity decay, with only 539.4 mAh g^{-1} and 623.2 mAh g^{-1} of specific discharge capacity maintained after 100 cycles. It is noted that the specific discharge capacity of TiO_2/CNFs is poor compared to that of CNFs after 40 cycles, which is due to the accumulation of solid sulfur species, resulting in buried catalytic centers and the formation of "dead" sulfur. At the initial stage, TiO_2 exhibits a higher polysulfide adsorption ability than CNFs and facilitates the catalysis of their redox conversion. As a result, the specific discharge capacity of TiO_2/CNFs is higher than that of CNFs. However, TiO_2, being a semiconductor, has limited electronic conductivity, leading to poor electron transfer from the catalytic center to the conductive carbon matrix. This results in the accumulation of solid sulfur species on the surface of TiO_2 particles, leading to reduced catalytically active sites and, consequently, inferior electrochemical performance. This further proves the significance of introducing oxygen vacancies to improve the electronic conductivity of TiO_2. The rate capabilities of the TiO_{2-x}/CNFs-based cathode at various current densities are shown in Fig. 5d. The specific discharge capacities decrease from 944.7 to 840.7, 784.8, and 710.4 mAh g^{-1} as the current density increases from 0.1 to 0.2, 0.5, and 1.0 C, respectively. Remarkably, when the current density is switched from 1.0 to 0.1 C, a high specific discharge capacity of 826.5 mAh g^{-1} is maintained, indicating the excellent capacity recoverability of the TiO_{2-x}/CNFs-based cathode. Furthermore, the long-term cycle performance of the TiO_{2-x}/CNFs-based cathode is evaluated at 0.5 C, as shown in Fig. 5e. The initial three cycles are conducted at a low current density to ensure the uniform and complete nucleation of LiPSs. The specific discharge capacity reaches 787.4 mAh g^{-1} at the forth cycle and remains stable at 584.0 mAh g^{-1} after 300 cycles, with high Coulombic efficiency (nearly 100%) and low-capacity decay (0.3% per cycle from the second cycle).

Based on the above analysis, it can be concluded that TiO_{2-x}/CNFs exhibit superior performance compared to TiO_2/CNFs and CNFs, and this can be attributed to the following reasons. First, the electrospun CNFs provide an electrically conductive framework that enables efficient electron transport within the entire electrode. This conductive framework facilitates rapid electron transfer during the redox reactions of lithium polysulfides, leading to enhanced electrochemical activity and overall battery performance. Second, the oxygen vacancy created by hydrogen reduction in TiO_{2-x}/CNFs plays a crucial role in enhancing the overall electrochemical performance. The presence of oxygen vacancies effectively improves the electrical conductivity of the TiO_{2-x} nanoparticles, ensuring a fast electron transfer from the catalytic center to the conductive carbon matrix.

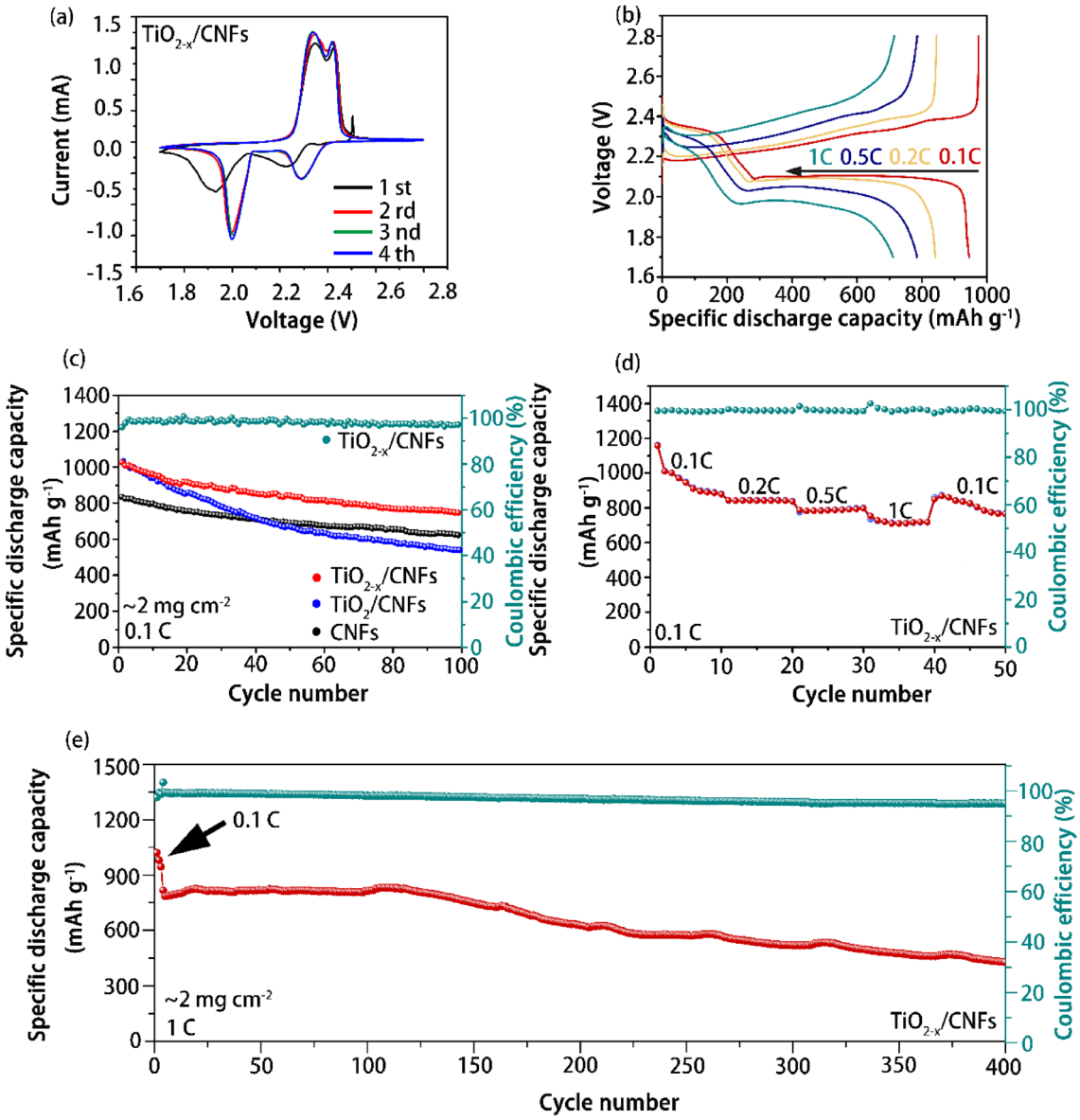

Fig. 5 **a** Cyclic voltammetry curves of the Li–S coin cells based on TiO_{2-x}/CNFs. **b** GCD plots of the coin cells based on TiO_{2-x}/CNFs at different current density. **c** Specific discharge capacity of the coin cells based on TiO_{2-x}/CNFs, TiO_2/CNFs, and CNFs-based cathode. **d** Rate performance of the Li–S coin cells based on TiO_{2-x}/CNFs. **e** Specific discharge capacity of the coin cells based on TiO_{2-x}/CNFs under a current density of 0.5C for 300 cycles (first three cycles at 0.1 C for activation)

The oxygen vacancy also enhances the polysulfides adsorption ability of TiO_{2-x}/CNFs, promoting the adsorption of LiPSs onto the electrode surface. Finally, the presence of polar TiO_{2-x} nanoparticles embedded in the CNFs provides nucleation sites for short-chain polysulfides, thus promoting their adsorption and conversion. Additionally, the polar nature of TiO_{2-x} suppresses the diffusion of long-chain polysulfides, preventing their migration and "shuttle effect" during battery cycling. Moreover, the polar TiO_{2-x} nanoparticles could guide the homogenous deposition/distribution of sulfur, which is another advantage of TiO_{2-x}/CNFs.

Synchrotron X-ray tomography was utilized to three-dimensionally (3D) visualize the (re)deposition by imaging the (re)distribution of sulfur during cycling. The assembled Li–S coin cells were galvanostatically cycled at 0.1 C with a sulfur loading of 1 mg cm^{-2} before stopping at the charged state at 2.8 V. The coin cells were then disassembled in the Ar-filled glove box, and the free-standing cathode electrodes after cycling were placed in an X-ray compatible sample container for X-ray tomography [64]. Figure 6a displays the spatial sulfur distribution after 1, 5, 10, 50, and 100 cycles within a sub-volume ($750 \times 770 \times 340$ μm^3) from the

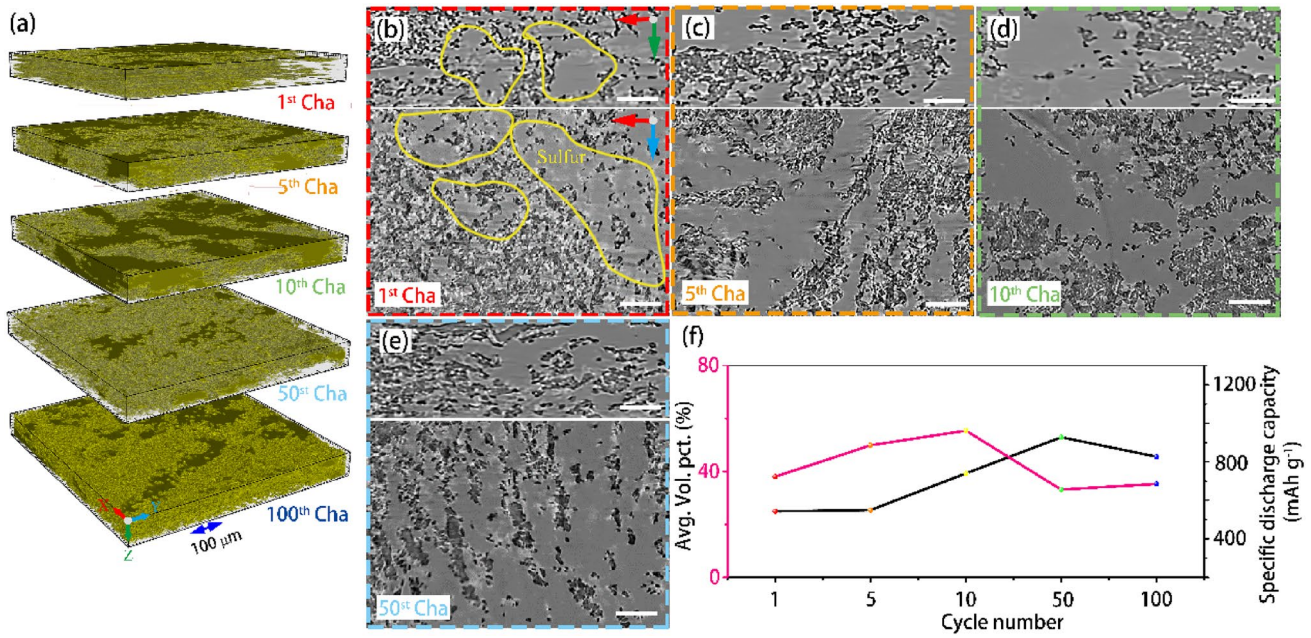

Fig. 6 **a** 3D rendering of the volume distribution of the sulfur deposition after different cycles; **b–e** x–y plane view (bottom) and the cross-section view (x–z plane, top) of the sulfur (re)deposition after different cycles. The scale bar for the x–y plane view (bottom) and cross-section view (top) is 50 μm and 100 μm, respectively. **f** The average volume percentage (left Y-axis, Avg. Vol. pct) of the sulfur within the composite cathode and the corresponding specific discharge capacity (right Y-axis, capacity) as a function of the cycling number

cathode composite. It is evident that sulfur tends to distribute across the whole composite electrode instead of aggregating locally. Additionally, the x–y plane and x–z plane views in Fig. 6b show the 2D distribution of sulfur (highlighted by yellow lines) after the first charge. With the proceeding of cycling, as shown in Fig. 6c–e and Fig. S12, similar distribution behavior of sulfur can be observed within the TiO_{2-x}/CNFs matrix after 5, 10, 50, and 100 cycles.

The spatial distribution of sulfur within the composite cathode is further quantified. As shown in Fig. S13, the volume percentage occupied by sulfur (across x–y plane) along z-axis in the sub-volume ($750 \times 770 \times 340$ μm^3) can be calculated, enabling the plotting of the volume percentage of sulfur along z-direction starting from separator to current collector (CC). After the first charge, the average volume/area percentage of sulfur within the x–y plane is approximately 39.0%, along z-direction without obvious fluctuations, suggesting a relative steady distribution of sulfur deposit along z-direction. In the following cycles, the volume percentage of sulfur gradually increased to 44.9% after the 5th charge and to 47.7% for the 10th charge. After that, the sulfur volume ratio decreased roughly to the initial level. The initial increase in the volume percentage of (re) deposited sulfur, observed before ten cycles, can be attributed to the growing number of nucleation sites during the early stages of cycling. The SEM images of the S/TiO_{2-x}/CNFs electrodes after 10th charge are shown in Fig. S14, from which it can be found that sulfur is homogenously coated on the TiO_{2-x}/CNFs. After 100 cycles, a homogenous volume percentage of sulfur (around 37.7%) along the z-direction (from the separator to the current collector) can be observed (Fig. 6f), indicating the homogeneous nucleation sites for sulfur deposition during extended cycling. To understand whether the uniform (re)deposition of sulfur is influenced by polar TiO_{2-x} nanoparticles or CNFs, the (re) distribution of sulfur in CNFs-based electrodes was imaged using Synchrotron X-ray tomography, as shown in Fig. S15. The sulfur exhibits a tendency to distribute homogeneously across the entire composite electrode without any local aggregation, even at different charge states. These findings strongly suggest that CNFs produced by electrospinning show promising potential as host materials for Li–S batteries, providing a facile approach to effectively regulate the precipitation of sulfur.

In the end, the free-standing property of the TiO_{2-x}/CNFs makes them good candidate for the application in flexible and wearable batteries. As proof of concept, a flexible Li–S pouch cell was assembled (Fig. 7a), consisting of free-standing TiO_{2-x}/CNFs as the host materials, Li_2S_8 solution (1 M) in DOL/DME as the catholyte, and lithium-coated Cu foil as the anode. The average mass loading of sulfur was approximately 2.0 mg cm^{-2}. The open-circuit potential (OCV) of the fresh pouch cell was stable at 2.3 V, even at a 90-degree bend state, indicating

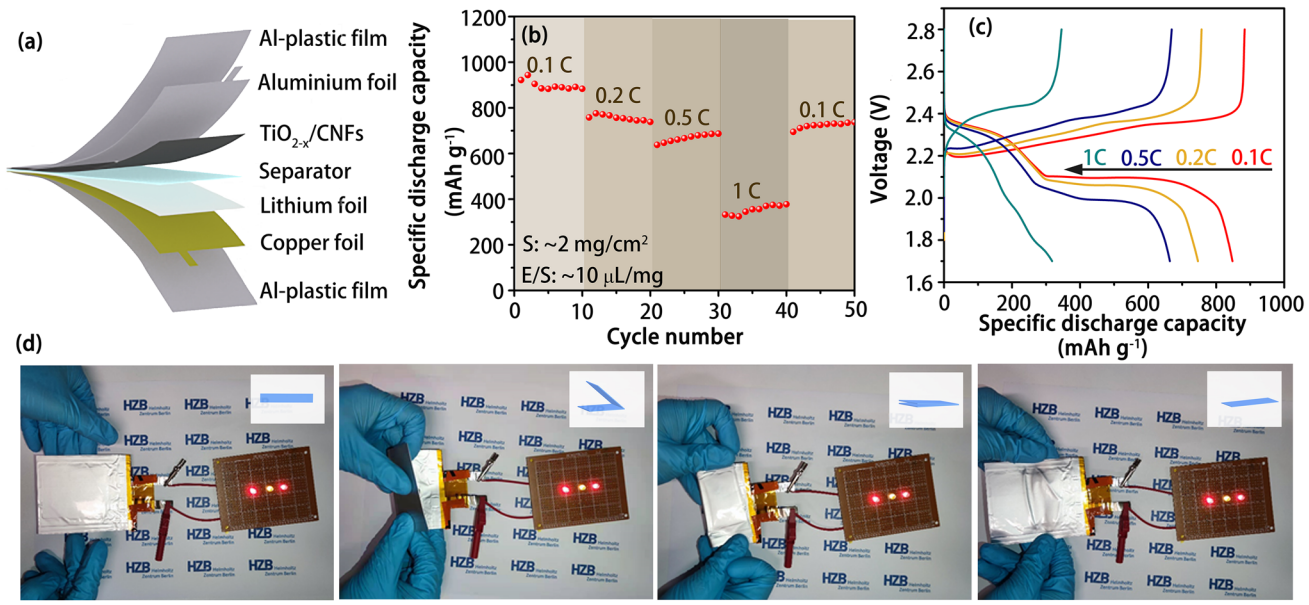

Fig. 7 **a** Illustration of the pouch cell configuration. **b** Rate performance and **c** galvanostatic charge–discharge (GCD) trends of the pouch cell based on TiO_{2-x}/CNFs-based cathode at different current densities of 0.1C, 0.2C, 0.5C, and 1C. **d** An LED panel consisting of 3 LED lights is powered by the assembled flexible pouch cell in various bent states

the high flexibility of the TiO_{2-x}/CNFs membrane (Fig. S16). Figure 7b shows the rate performances of the Li–S pouch cell at different current densities (0.1 C, 0.2 C, 0.5 C, and 1.0 C) and then returning to 0.1 C. The pouch cell exhibited high reversible discharge capacities of 847.4, 745.9, 663.2, and 351.5 mAh g^{-1} at 0.1 C, 0.2 C, 0.5 C, and 1.0 C, respectively. When the current density returned to 0.1C, a discharge capacity of 698.0 mAh g^{-1} could still be recovered, indicating its good rate capacity. The corresponding galvanostatic charge/discharge profiles at different current densities are shown in Fig. 7c, featuring a two-step discharge and two merging charge profiles, similar to that of the coin cells. To showcase practical applications, a light-emitting diode (LED) panel consisting of three LED lights was powered by the assembled flexible pouch cell. Digital images of the LED lights powered by the flexible pouch cell bent at different degrees are displayed in Fig. 7d. The unchanged LED light intensity at different bent states demonstrates the potential of TiO_{2-x}/CNFs electrode for wearable energy storage applications. The flexibility and excellent electrochemical performance of the free-standing TiO_{2-x}/CNFs-based cathode make it a promising candidate for wearable and flexible energy storage devices.

Conclusion

In conclusion, we successfully prepared a flexible and free-standing TiO_{2-x}/CNFs electrode using a facile two-step method. The TiO_{2-x} nanoparticles were uniformly embedded in the CNFs without aggregation, resulting in abundant exposed active sites and improved electrical conductivity. X-ray diffraction (XRD) analysis confirmed the presence of both anatase and rutile phases in TiO_{2-x}/CNFs, which could be controlled by varying the calcination temperature. The hybrid anatase/rutile phase of TiO_2 in TiO_{2-x}/CNFs exhibits a synergistic effect, effectively suppressing the shuttle effect of lithium polysulfides and enhancing the redox kinetics during LiPSs' conversion reactions, as confirmed both by experiments and DFT calculations. As a result, Li–S coin cells with TiO_{2-x}/CNFs-based cathode delivered an initial specific discharge capacity of 787.4 mAh g^{-1} at 0.5 C and this capacity can be maintained at 584.0 mAh g^{-1} after 300 cycles. The uniform and homogenous distribution of sulfur during cycling, as revealed by synchrotron X-ray tomography, indicates the role of TiO_{2-x}/CNFs in regulating sulfur deposition. Moreover, the free-standing nature of TiO_{2-x}/CNFs made it suitable for flexible batteries applications, demonstrating its potential in practical usage scenarios. Therefore, the incorporation of hybrid anatase/rutile phase

TiO_{2-x} nanoparticles into free-standing carbon nanofibers provides a synergistic effect, making it a potential solution for addressing the challenges associated with lithium polysulfides and improving the overall performance of lithium–sulfur batteries.

Supplementary Information The online version contains supplementary material available at https://doi.org/10.1007/s42765-024-00380-1.

Acknowledgements The authors thank the Open Project of State Key Laboratory for Modification of Chemical Fibers and Polymer Materials, Donghua University (Grant No. LK1702). PF acknowledges financial support of CSC scholarship (No. 202006630007). The authors would acknowledge BESSY II at Helmholtz-Zentrum Berlin for the beam time allocation at BAMline. The authors thank Dongjiu Xie at Helmholtz-Zentrum Berlin for collecting the BET results.

Funding Open Access funding enabled and organized by Projekt DEAL. This article is funded by China Scholarship Council, 202006630007, Ping Feng, State Key Laboratory for Modification of Chemical Fibers and Polymer Materials, LK1702.

Data availability The data that support the findings of this study are available from the corresponding author upon reasonable request.

Declarations

Conflict of Interest YL and MFZ are the Editorial Board Member/Editor-in-Chief for Advanced Fiber Materials and were not involved in the editorial review or the decision to publish this article. All authors declare that there are no competing interests.

References

1. Bruce Dunn HK. Jean-Marie tarascon, electrical energy storage for the grid: a battery of choices. *Science*. **2011**;*334*:928–35.
2. Qi Y, Li Q-J, Wu Y, Bao S-J, Li C, Chen Y, Wang G, Xu M. A Fe3N/carbon composite electrocatalyst for effective polysulfides regulation in room-temperature Na-S batteries. *Nat Commun*. **2021**. https://doi.org/10.1038/s41467-021-26631-y.
3. Zhu X, Zhang Y, Man Z, Lu W, Chen W, Xu J, Bao N, Chen W, Wu G. Microfluidic-assembled covalent organic Frameworks@ Ti3C2Tx MXene vertical fibers for high-performance electrochemical supercapacitors. *Adv Mater*. **2023**. https://doi.org/10.1002/adma.202307186.
4. Cheng Z, Xiao Z, Pan H, Wang S, Wang R. Elastic sandwich-type rGO–VS2/S composites with high tap density: structural and chemical cooperativity enabling lithium–sulfur batteries with high energy density. *Adv Energy Mater*. **2017**. https://doi.org/10.1002/aenm.201702337.
5. Liu Y, Zhao M, Hou LP, Li Z, Bi CX, Chen ZX, Cheng Q, Zhang XQ, Li BQ, Kaskel S, Huang JQ. An organodiselenide comediator to facilitate sulfur redox kinetics in lithium–sulfur batteries with encapsulating lithium polysulfide electrolyte. *Angewandte Chemie Int Ed*. **2023**. https://doi.org/10.1002/anie.202303363.
6. Liao Y, Yuan L, Liu X, Meng J, Zhang W, Li Z, Huang Y. Low-cost fumed silicon dioxide uniform Li+ flux for lean-electrolyte and anode-free Li/S battery. *Energy Storage Mater*. **2022**;*48*:366–74.
7. Danuta H, Juliusz U, US Patent No. 3,043,896. Washington, DC: U.S. Patent and Trademark Office. 1962.
8. Wang P, Xi B, Zhang Z, Huang M, Feng J, Xiong S. Atomic tungsten on graphene with unique coordination enabling kinetically boosted lithium–sulfur batteries. *Angew Chem Int Ed*. **2021**;*60*(28):15563–71.
9. Zhang C, Du R, Biendicho JJ, Yi M, Xiao K, Yang D, Zhang T, Wang X, Arbiol J, Llorca J, Zhou Y, Morante JR, Cabot A. Tubular CoFeP@CN as a Mott-Schottky catalyst with multiple adsorption sites for robust lithium−sulfur batteries. *Adv Energy Mater*. **2021**;*11*(24):2100432.
10. Zhao C, Xu GL, Yu Z, Zhang L, Hwang I, Mo YX, Ren Y, Cheng L, Sun CJ, Ren Y, Zuo X, Li JT, Sun SG, Amine K, Zhao T. A high-energy and long-cycling lithium–sulfur pouch cell via a macroporous catalytic cathode with double-end binding sites. *Nat Nanotechnol*. **2021**;*16*(2):166–73.
11. Kim JT, Hao X, Wang C, Sun X. Cathode materials for single-phase solid-solid conversion Li-S batteries. *Matter*. **2023**;*6*(2):316–43.
12. Cai D, Liu B, Zhu D, Chen D, Lu M, Cao J, Wang Y, Huang W, Shao Y, Tu H, Han W. Ultrafine Co3Se4 nanoparticles in nitrogen-doped 3D carbon matrix for high-stable and long-cycle-life lithium sulfur batteries. *Adv Energy Mater*. **2020**;*10*(19):1904273.
13. Ye Z, Jiang Y, Li L, Wu F, Chen R. Self-assembly of 0D–2D heterostructure electrocatalyst from MOF and MXene for boosted lithium polysulfide conversion reaction. *Adv Mater*. **2021**;*33*(33):e2101204.
14. Xie Y, Cao J, Wang X, Li W, Deng L, Ma S, Zhang H, Guan C, Huang W. MOF-derived bifunctional Co0.85Se nanoparticles embedded in N-doped carbon nanosheet arrays as efficient sulfur hosts for lithium–sulfur batteries. *Nano Lett*. **2021**;*21*(20):8579–86.
15. Raza H, Bai S, Cheng J, Majumder S, Zhu H, Liu Q, Zheng G, Li X, Chen G. Li-S batteries: challenges, achievements and opportunities. *Electrochem Energy Rev*. **2023**. https://doi.org/10.1007/s41918-023-00188-4.
16. Ilango PR, Savariraj AD, Huang H, Li L, Hu G, Wang H, Hou X, Kim BC, Ramakrishna S, Peng S. Electrospun flexible nanofibres for batteries: design and application. *Electrochem Energy Rev*. **2023**. https://doi.org/10.1007/s41918-022-00148-4.
17. Chung SH, Chang CH, Manthiram A. Progress on the critical parameters for lithium–sulfur batteries to be practically viable. *Adv Funct Mater*. **2018**;*28*(28):1801188.
18. Feng T, Zhao T, Zhang N, Duan Y, Li L, Wu F, Chen R. 2D Amorphous Mo-Doped CoB for bidirectional sulfur catalysis in lithium sulfur batteries. *Adv Func Mater*. **2022**;*32*(30):2202766.
19. Gueon D, Ju MY, Moon JH. Complete encapsulation of sulfur through interfacial energy control of sulfur solutions for high-performance Li-S batteries. *Proc Natl Acad Sci USA*. **2020**;*117*(23):12686–92.
20. Xie D, Mei S, Xu Y, Quan T, Hark E, Kochovski Z, Lu Y. Efficient sulfur host based on yolk-shell iron oxide/sulfide-carbon nanospindles for lithium–sulfur batteries. *Chemsuschem*. **2021**;*14*(5):1404–13.

21. Deng R, Ke B, Xie Y, Cheng S, Zhang C, Zhang H, Lu B, Wang X. All-solid-state thin-film lithium–sulfur batteries. *Nano-Micro Lett*. **2023**. https://doi.org/10.1007/s40820-023-01064-y.
22. Yang Y, Zheng G, Cui Y. Nanostructured sulfur cathodes. *Chem Soc Rev*. **2013**;*42*(7):3018–32.
23. Liang X, Rangom Y, Kwok CY, Pang Q, Nazar LF. Interwoven MXene Nanosheet/carbon-nanotube composites as Li-S cathode hosts. *Adv Mater*. **2017**. https://doi.org/10.1002/adma.201603040.
24. Xiao K, Wang J, Chen Z, Qian Y, Liu Z, Zhang L, Chen X, Liu J, Fan X, Shen ZX. Improving polysulfides adsorption and redox kinetics by the Co(4) N nanoparticle/N-doped carbon composites for lithium–sulfur batteries. *Small*. **2019**;*15*(25): e1901454.
25. Ao J, Xie Y, Lai Y, Yang M, Xu J, Wu F, Cheng S, Wang X. CoSe2 nanoparticles-decorated carbon nanofibers as a hierarchical self-supported sulfur host for high-energy lithium–sulfur batteries. *Sci China Mater*. **2023**;*66*(8):3075–83.
26. Zielke L, Barchasz C, Walus S, Alloin F, Lepretre JC, Spettl A, Schmidt V, Hilger A, Manke I, Banhart J, Zengerle R, Thiele S. Degradation of Li/S battery electrodes on 3D current collectors studied using X-ray phase contrast tomography. *Sci Rep*. **2015**;*5*:10921.
27. Yermukhambetova A, Tan C, Daemi SR, Bakenov Z, Darr JA, Brett DJ, Shearing PR. Exploring 3D microstructural evolution in Li-Sulfur battery electrodes using in-situ X-ray tomography. *Sci Rep*. **2016**;*6*:35291.
28. Yang D, Liang Z, Tang P, Zhang C, Tang M, Li Q, Biendicho JJ, Li J, Heggen M, Dunin-Borkowski RE, Xu M, Llorca J, Arbiol J, Morante JR, Chou SL, Cabot A. A high conductivity 1D pi-d conjugated metal-organic framework with efficient polysulfide trapping-diffusion-catalysis in lithium–sulfur batteries. *Adv Mater*. **2022**. https://doi.org/10.1002/adma.202108835.
29. Mei S, Jafta CJ, Lauermann I, Ran Q, Kärgell M, Ballauff M, Lu Y. Porous Ti4O7Particles with interconnected-pore structure as a high-efficiency polysulfide mediator for lithium–sulfur batteries. *Adv Funct Mater*. **2017**;*27*(26):1701176.
30. Mei S, Siebert A, Xu Y, Quan T, Garcia-Diez R, Bär M, Härtel P, Abendroth T, Dörfler S, Kaskel S, Lu Y. Large-scale synthesis of nanostructured carbon-Ti4O7 hollow particles as efficient sulfur host materials for multilayer lithium–sulfur pouch cells. *Batter Supercaps*. **2022**. https://doi.org/10.1002/batt.202100398.
31. Xie D, Xu Y, Wang Y, Pan X, Härk E, Kochovski Z, Eljarrat A, Müller J, Koch CT, Yuan J, Lu Y. Poly(ionic liquid) nanovesicle-templated carbon nanocapsules functionalized with uniform iron nitride nanoparticles as catalytic sulfur host for Li–S batteries. *ACS Nano*. **2022**;*16*(7):10554–65.
32. Zhang Y, Wang Y, Luo R, Yang Y, Lu Y, Guo Y, Liu X, Cao S, Kim JK, Luo Y. A 3D porous FeP/rGO modulated separator as a dual-function polysulfide barrier for high-performance lithium sulfur batteries. *Nanoscale Horiz*. **2020**;*5*(3):530–40.
33. Guo Y, Li J, Pitcheri R, Zhu J, Wen P, Qiu Y. Electrospun Ti4O7/C conductive nanofibers as interlayer for lithium–sulfur batteries with ultra long cycle life and high-rate capability. *Chem Eng J*. **2019**;*355*:390–8.
34. Jiao L, Zhang C, Geng C, Wu S, Li H, Lv W, Tao Y, Chen Z, Zhou G, Li J, Ling G, Wan Y, Yang QH. Capture and catalytic conversion of polysulfides by in situ built TiO2-MXene heterostructures for lithium–sulfur batteries. *Adv Energy Mater*. **2019**;*9*(19):1900219.
35. Chen Z, Hu Y, Liu W, Yu F, Yu X, Mei T, Yu L, Wang X. Three-dimensional engineering of sulfur/MnO2 composites for high-rate lithium–sulfur batteries. *ACS Appl Mater Interfaces*. **2021**;*13*(32):38394–404.
36. Chung S-H, Luo L, Manthiram A. TiS2–polysulfide hybrid cathode with high sulfur loading and low electrolyte consumption for lithium–sulfur batteries. *ACS Energy Lett*. **2018**;*3*(3):568–73.
37. Lang X, Zhao Y, Cai K, Li L, Chen D, Zhang Q. A facile synthesis of stable TiO2/TiC composite material as sulfur immobilizers for cathodes of lithium–sulfur batteries with excellent electrochemical performances. *Energ Technol*. **2019**;*7*(12):1900543.
38. Ni J, Jin L, Xue M, Zheng J, Zheng JP, Zhang C. TiO2 microboxes as effective polysufide reservoirs for lithium sulfur batteries. *Electrochim Acta*. **2019**;*296*:39–48.
39. Yin Z, Zhang X, Cai Y, Chen J, Wong JI, Tay YY, Chai J, Wu J, Zeng Z, Zheng B, Yang HY, Zhang H. Preparation of MoS2–MoO3 hybrid nanomaterials for light-emitting diodes. *Angew Chem Int Ed*. **2014**;*53*(46):12560–5.
40. Gao P, Chen Z, Gong Y, Zhang R, Liu H, Tang P, Chen X, Passerini S, Liu J. The role of cation vacancies in electrode materials for enhanced electrochemical energy storage: synthesis, advanced characterization, and fundamentals. *Adv Energy Mater*. **2020**. https://doi.org/10.1002/aenm.201903780.
41. Zhang Y, Ding Z, Foster CW, Banks CE, Qiu X, Ji X. Oxygen vacancies evoked blue TiO2(B) nanobelts with efficiency enhancement in sodium storage behaviors. *Adv Funct Mater*. **2017**;*27*(27):1700856.
42. Wang H, Zhang J, Hang X, Zhang X, Xie J, Pan B, Xie Y. Half-metallicity in single-layered manganese dioxide nanosheets by defect engineering. *Angew Chem Int Ed*. **2014**;*54*(4):1195–9.
43. Hao Z, Chen Q, Dai W, Ren Y, Zhou Y, Yang J, Xie S, Shen Y, Wu J, Chen W, Xu GQ. Oxygen-deficient blue TiO2 for ultrastable and fast lithium storage. *Adv Energy Mater*. **2020**;*10*(10):1903107.
44. Liang Z, Zheng G, Li W, Seh ZW, Yao H, Yan K, Cui Y. Sulfur cathodes with hydrogen reduced titanium dioxide inverse opal structure. *ACS Nano*. **2014**;*8*:5249.
45. Wang HC, Fan CY, Zheng YP, Zhang XH, Li WH, Liu SY, Sun HZ, Zhang JP, Sun LN, Wu XL. Oxygen-deficient titanium dioxide nanosheets as more effective polysulfide reservoirs for lithium–sulfur batteries. *Chemistry*. **2017**;*23*(40):9666–73.
46. Wang H-E, Yin K, Qin N, Zhao X, Xia F-J, Hu Z-Y, Guo G, Cao G, Zhang W. Oxygen-deficient titanium dioxide as a functional host for lithium–sulfur batteries. *J Mater Chem A*. **2019**;*7*(17):10346–53.
47. Yao S, Zhang C, Xie F, Xue S, Gao K, Guo R, Shen X, Li T, Qin S. Hybrid membrane with SnS2 nanoplates decorated nitrogen-doped carbon nanofibers as binder-free electrodes with ultrahigh sulfur loading for lithium sulfur batteries. *ACS Sustain Chem Eng*. **2020**;*8*(7):2707–15.
48. Zhang X, Liu X, Zhang W, Song Y. Tunable vacancy defect chemistry on free-standing carbon cathode for lithium–sulfur batteries. *Green Energy Environ*. **2023**;*8*(2):354–9.
49. Yang Z, Peng C, Meng R, Zu L, Feng Y, Chen B, Mi Y, Zhang C, Yang J. Hybrid anatase/rutile nanodots-embedded covalent organic frameworks with complementary polysulfide adsorption for high-performance lithium–sulfur batteries. *ACS Cent Sci*. **2019**;*5*(11):1876–83.
50. Salhabi EHM, Zhao J, Wang J, Yang M, Wang B, Wang D. Hollow multi-shelled structural TiO2-x with multiple spatial confinement for long-life lithium–sulfur batteries. *Angew Chem Int Ed Engl*. **2019**;*58*(27):9078–82.
51. Cheng H, Selloni A. Surface and subsurface oxygen vacancies in anataseTiO2and differences with rutile. *Phys Rev B*. **2009**. https://doi.org/10.1103/PhysRevB.79.092101.
52. Cui Z, He SA, Liu Q, Guan G, Zhang W, Xu C, Zhu J, Feng P, Hu J, Zou R, Zhu M. Graphene-like carbon film wrapped tin (II) sulfide nanosheet arrays on porous carbon fibers with enhanced electrochemical kinetics as high-performance Li and Na ion battery anodes. *Adv Sci*. **2020**. https://doi.org/10.1002/advs.201903045.
53. Cao X, Chen W, Zhao P, Yang Y, Yu DG. Electrospun porous nanofibers: pore-forming mechanisms and applications for

photocatalytic degradation of organic pollutants in wastewater. *Polymers (Basel)*. **2022**;*14*(19):3990.
54. Liu Y, Qin X, Zhang S, Liang G, Kang F, Chen G, Li B. Fe3O4-decorated porous graphene interlayer for high-performance lithium–sulfur batteries. *ACS Appl Mater Interfaces*. **2018**;*10*(31):26264–73.
55. Geng P, Wang L, Du M, Bai Y, Li W, Liu Y, Chen S, Braunstein P, Xu Q, Pang H. MIL-96-Al for Li–S batteries: shape or size? *Adv Mater*. **2021**;*34*(4):2107836.
56. Liu W, Luo C, Zhang S, Zhang B, Ma J, Wang X, Liu W, Li Z, Yang Q-H, Lv W. Cobalt-doping of molybdenum disulfide for enhanced catalytic polysulfide conversion in lithium–sulfur batteries. *ACS Nano*. **2021**;*15*(4):7491–9.
57. Wang R, Wu R, Yan X, Liu D, Guo P, Li W, Pan H. Implanting single Zn atoms coupled with metallic Co nanoparticles into porous carbon nanosheets grafted with carbon nanotubes for high-performance lithium–sulfur batteries. *Adv Funct Mater*. **2022**;*32*(20):2200424.
58. Jia H, Nandy A, Liu M, Kulik HJ. Modeling the roles of rigidity and dopants in single-atom methane-to-methanol catalysts. *J Mater Chem A*. **2022**;*10*(11):6193–203.
59. Li Z, Zhou Y, Wang Y, Lu Y-C. Solvent-mediated Li2S electrodeposition: a critical manipulator in lithium–sulfur batteries. *Adv Energy Mater*. **2019**;*9*(1):1802207.
60. Fan FY, Carter WC, Chiang YM. Mechanism and kinetics of Li2S precipitation in lithium–sulfur batteries. *Adv Mater*. **2015**;*27*(35):5203–9.
61. Zhang S, Ao X, Huang J, Wei B, Zhai Y, Zhai D, Deng W, Su C, Wang D, Li Y. Isolated single-atom Ni–N5 catalytic site in hollow porous carbon capsules for efficient lithium–sulfur batteries. *Nano Lett*. **2021**;*21*(22):9691–8.
62. Du M, Geng P, Pei C, Jiang X, Shan Y, Hu W, Ni L, Pang H. High-entropy prussian blue analogues and their oxide family as sulfur hosts for lithium–sulfur batteries. *Angewandte Chemie Int Ed*. **2022**. https://doi.org/10.1002/anie.202209350.
63. Sun T, Zhao X, Li B, Shu H, Luo L, Xia W, Chen M, Zeng P, Yang X, Gao P, Pei Y, Wang X. NiMoO4 nanosheets anchored on NS doped carbon clothes with hierarchical structure as a bidirectional catalyst toward accelerating polysulfides conversion for LiS battery. *Adv Func Mater*. **2021**;*31*(25):2101285.
64. Dong K, Osenberg M, Sun F, Markötter H, Jafta CJ, Hilger A, Arlt T, Banhart J, Manke I. Non-destructive characterization of lithium deposition at the Li/separator and Li/carbon matrix interregion by synchrotron X-ray tomography. *Nano Energy*. **2019**;*62*:11–9.